# High-flux wavelength tunable XUV source in the 12–40.8 eV photon energy range with adjustable energy and time resolution for Tr-ARPES applications

JI WANG,[1,2,7] FAMIN CHEN,[1,3,7] MOJUN PAN,[1,3] SIYUAN XU,[1,4,5] RENCHONG LV,[1,4] JUNDE LIU,[1,3] YUANFENG LI,[1,4] SHAOBO FANG,[1,3,6] YUNLIN CHEN,[2] JIANGFENG ZHU,[4] DACHENG ZHANG,[4] TIAN QIAN,[1,8] CHENXIA YUN,[1,9] KUN ZHAO,[1,6,10] HONG DING,[1] AND ZHIYI WEI[1,3,6,11]

[1]*Beijing National Laboratory for Condensed Matter Physics, Institute of Physics, Chinese Academy of Sciences, Beijing 100190, China*
[2]*Institute of Applied Mic-Nano Materials, School of Science, Beijing Jiaotong University, Beijing 100044, China*
[3]*Department of Physics, University of Chinese Academy of Sciences, Beijing 100049, China*
[4]*School of Physics and Optoelectronic Engineering, Xidian University, Xi'an 710071, China*
[5]*Institute of Photonics & Photon-Technology, School of Physics, Northwest University, Xi'an 710069, China*
[6]*Songshan Lake Materials Laboratory, Dongguan 523808, China*
[7]*Equal contributors.*
[8]*tqian@iphy.ac.cn*
[9]*cxyun@iphy.ac.cn*
[10]*zhaokun@iphy.ac.cn*
[11]*zywei@iphy.ac.cn*

**Abstract:** High-order harmonic generation (HHG) has a broad spectrum covering vacuum ultraviolet to extreme ultraviolet (XUV) bands, which is useful for applications involving material analyses at different information depths. Such an HHG light source is perfect for time- and angle-resolved photoemission spectroscopy. Here, we demonstrate a high-photon flux HHG source driven by a two-color field. Applying a fused silica compression stage to reduce the driving pulse width, we obtained a high XUV photon flux of $2 \times 10^{12}$ phs/s @21.6 eV on target. We designed a classical diffraction mounted (CDM) grating monochromator that can achieve a wide range of photon energy from 12 to 40.8 eV, while the time resolution is improved by reducing the pulse front tilt after the harmonic selection. We designed a spatial filtering method to adjust the time resolution using the CDM monochromator and significantly reduced the pulse front tilt of the XUV pulses. We also demonstrate a detailed prediction of the energy resolution broadening which is caused by the space charge effect.

## 1. Introduction

Time- and angle-resolved photoemission spectroscopy (time-resolved ARPES or Tr-ARPES) is a powerful tool for studying the band structure and non-equilibrium dynamics of condensed matters [1,2]. The Tr-ARPES experiments need a coherent vacuum ultraviolet (VUV), extreme ultraviolet (XUV), or soft X-ray source with pump-probe detection to measure the energy-momentum dispersion relationship of materials and investigate the electron dynamics [3]. A light source tunable from VUV to XUV brings depth selectivity since the electron escape depth depends on the kinetic energy of the photoelectrons [4]. The VUV or soft X-ray source enables bulk-sensitive measurements [5,6], while the XUV source around 30 eV enables surface-sensitive measurements

[7]. At present, soft X-ray sources are the most commonly used to proceed bulk-sensitive measurements which are generated by synchrotron radiation [6,8]. The VUV sources generated by frequency doubling are also used to obtain bulk information [5]. However, the photon energy in this technique is limited up to 7 eV, with which it is difficult to cover the entire Brillouin zone [9]. Recent researches address this problem by increasing the photon energy of the laser source to 10-11 eV [10,11]. Using a light source with photon energy covering 10~30 eV, the depth selection between the surface and multi atomic layers can be performed. Therefore, the energy dispersion along the normal direction of the three-dimensional structures can be explored [12]. There are several XUV wavelength selection methods that are applied in Tr-ARPES such as wavelength selection via monochromator or via filters (for example, aluminum foils or XUV mirrors). A monochromator can select the photon energy continuously, but the grating in a monochromator brings pulse front tilt, which spatially chirps the XUV pulses and makes the time resolution worse. The pulse front tilt can be reduced by using an off-plane mount (OPM) scheme [13] instead of using the conventional diffraction mount (CDM) scheme. However, the OPM mount has a much narrower tuning range than the CDM scheme, so it can hardly cover the range from VUV to XUV. An XUV filter, often an aluminum or a tin foil, can block the higher photon energy components without inducing pulse front tilt. The bandwidth of an XUV filter is generally large, and the energy selection is hard to control. There are also probably some other components with lower photon energies than the selected component passing through the filter [14], which is usually harmless in an ARPES measurement. Still, the extra photons in the XUV pulses bring a more significant space charge effect.

High-order harmonic generation (HHG) is one of the well-known methods to generate coherent XUV sources. An XUV source with a high photon number per pulse can perform fast measurements. However, it also brings serious space charge effect and affects the energy resolution of the system [15]. A solution is driving the HHG at higher repetition rates to reduce the photon number per pulse. If the laser output power stays the same, the energy per pulse is reduced by a factor N when the repetition rate is increased by N times. However, due to the nonlinear effect in HHG, the XUV photons per pulse will be reduced by a factor much larger than N. Therefore, the HHG efficiency needs to be improved to achieve the same or even higher photon flux per second to keep the signal collection time in experiments the same or shorter. Here the photon flux is described as the average photon number per second. In many studies, two-color driving fields are used to enhance the conversion efficiency of HHG [16,17,18], which have not been examined in generating XUV sources for Tr-ARPES yet. However, although the increase in repetition rate allows larger photon flux in time-resolved measurements, the space charge effect is still inevitable in single-pass HHG sources, of which repetition rates are below megahertz.

To this end, we demonstrate a high photon flux, broadband wavelength tunable XUV source in which the pulse front tilt has been reduced. A two-color driving field compressed by fused silica plates is used to generate harmonics at high efficiency and with a broad bandwidth. The properties of two-color field driven harmonics are also investigated. To achieve the broadband wavelength selection, a monochromator in the CDM instead of in the OPM is applied in the beamline. We have thoroughly analyzed the pulse front tilt and the space charge effect in this system, and we use a spatial filtering method to overcome the significant pulse front tilt caused by the grating while reducing the space charge effect. In our experiment, the system achieved an energy resolution of 96 meV and a time resolution of 110 fs, breaking through the limitation of the time resolution in unmodified CDM. Additionally, our modeling and simulation with the Monte Carlo method to the space charge effect shows results consistent with earlier studies [19,20]. We also employ a differential pumping design in the vacuum system to maintain extremely high vacuum in the ARPES analyzer. This wide-range tunable XUV source shows the probability to proceed fast and accurate nonequilibrium measurements with depth selectivity. The photon energy of this XUV source covers 12~40.8 eV, and the maximum photon flux at the sample reaches $2 \times 10^{12}$

phs/s@21.6 eV. This high-flux result is achieved not only by a high HHG efficiency driven by two-color pulses but also a high transmission efficiency of our beamline. Especially, our simple and compact CDM monochromator achieves a relatively high transmission, while the pulse front tilt effect can be controlled and reduced by the out-of-focus slits. In comparison, most of the HHG sources for tr-ARPES have fluxes of $1 \times 10^{10} \sim 5 \times 10^{11}$ phs/s at the sample [1,9,14,19,20,21,22].

## 2. HHG source

### 2.1. High repetition rate laser system

The Tr-ARPES experiment requires a high repetition rate, high flux XUV source which is generated by a driving laser at the same repetition rate. A high XUV photon flux can be easily obtained by a proper laser at a low repetition rate. However, XUV sources with low repetition rates and high photon fluxes bring significant space charge effect that leads to an energy broadening. HHG driven by high repetition rate lasers can overcome this shortcoming. By reducing the XUV photon number in each pulse, the XUV source with a high repetition rate can provide sufficient photon flux to support ARPES experiments while minimizing the space charge effect.

The laser source used in our setup is a commercial high repetition rate fiber laser (Active Fiber GmbH). The amplifier generates 350 fs pulses at 1030 nm and the repetition rate is adjustable from 50 kHz to 19.1 MHz. The maximum single pulse energy is amplified to 100 μJ by chirped pulse amplification (CPA) with a 50 kHz ∼ 800 kHz repetition rate. The seed pulse is selected by a Pockels cell, and then the amplified pulses are sent to the hollow-core fiber compression stage. A 1-meter-long hollow-core fiber with a 250 μm diameter core filled with 13 bar krypton is used for spectrum broadening. Self-phase modulation in high-density krypton extends the spectral width from 6.8 nm to 70 nm. The broadened pulse is then compressed by chirped mirrors. The output single pulse energy is about 50 μJ, the pulse duration is less than 50 fs, and the overall compression efficiency is about 50%. The average power of the CPA output is 40 W at 400 kHz repetition rate, and the power becomes 20 W after the hollow-core fiber compression stage.

In experiments, most of the laser power is used to generate XUV photons. However, pump-probe experiments require infrared pulses at the sample to initiate a non-equilibrium process. A 5:95 beam splitter is used to distribute about 2.5 μJ pulse energy to the pump beam and 47.5 μJ pulse energy to the HHG beamline. The beam waist radius of the pump beam at the sample is adjusted to 300 μm so that the maximum intensity of the pump is about 1.8 mJ/cm$^2$.

### 2.2. Pulse compression using fused silica plates

Frequency doubling is the first step to producing the two-color driving field, which enhances HHG efficiency. However, the frequency up-conversion process and the absorption of optical elements bring significant energy loss. The reduced pulse energy leads to the need to adopt a tighter focusing geometry in HHG, which causes a more demanding phase matching requirement [23].

The phase matching condition can be improved by enhancing the laser intensity via further pulse compression [23]. We build a secondary compression stage based on fused silica plates [24,25,26] before the frequency doubling operation. The beam split to the HHG arm is focused by a f = 500 mm lens, and here we mark the focal plane as z = 0. Four 600-μm thick fused silica plates are then placed at z = -75 mm, z = -65 mm, z = 25 mm and z = 35 mm, respectively. Each fused silica plate is set at the Brewster's angle. The laser spectrum is broadened via self-phase modulation (SPM) in fused silica plates from 990 ∼ 1070 nm to 910 ∼ 1090 nm, as shown in Fig. 1.

The beam after the fused silica plates is collimated by a f = 750 mm silver-coated concave mirror. The shortest pulse duration after this secondary compression is 20 fs as shown in Fig. 2(a), where the dispersion compensation is realized by three pairs of chirped mirrors. The Fourier-transform
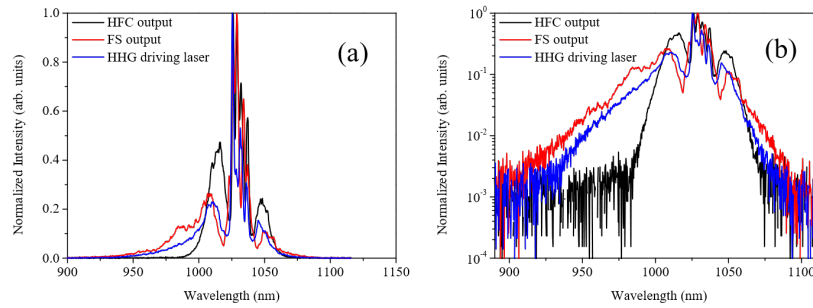
**Fig. 1.** The spectra of the laser output in (a) linear scale (b) log scale. Black lines: spectrum after the hollow-core fiber compression. Red lines: spectrum after the fused silica compression. Blue lines: spectrum before the HHG gas jet.

limit pulse duration of the broadened spectrum is 16.8 fs. Each pair of the chirped mirrors provide a group delay dispersion (GDD) of -60 fs$^2$. The pulse duration is measured using Second Harmonic Generation - Frequency Resolved Optical Gating (SHG-FROG) method. An additional pair of chirped mirrors are used to pre-compensate the dispersion of the air during propagation. For HHG we expanded the pulse duration to 26.2 fs to reduce the side pulses by adjusting the distance of the fused silica plates to the focal plane, as shown in Fig. 2(b). The pulse duration in this case is close to its Fourier-transform limit 26.19 fs.
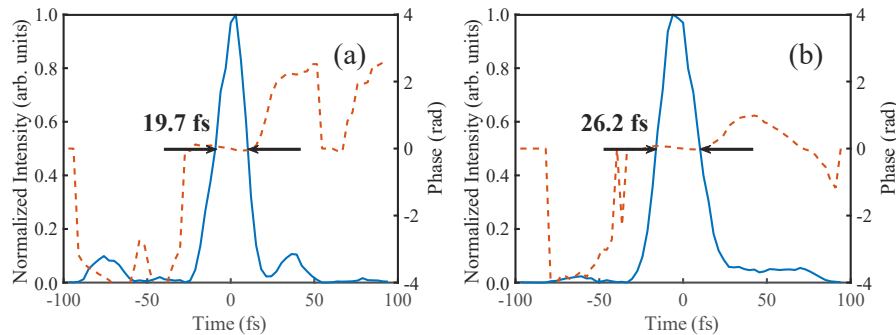


**Fig. 2.** The pulse duration after compression. (a) The shortest pulse duration (b) The pulse duration used for HHG.

The average power is reduced from 20 W to 18 W after the laser passing through the fused silica plates and is further reduced to 15 W after being compressed by three pairs of chirped mirrors. Although the fused silica plates provide stable spectral broadening and avoid the severe plasma and thermal effects in bulk materials, the thermal effects become obvious in fused silica plates at a higher repetition rate. In our experiment, when the repetition rate is 600 kHz or higher, the thermal effect in the fused silica plates becomes significant. When the laser runs at above 600 kHz, the high-efficiency HHG lasts only a few seconds, then its conversion efficiency drops dramatically. Therefore, we continue our experiments at a repetition rate of 400 kHz.

## 2.3. HHG and the XUV beamline

High-efficiency HHG is achieved by using a two-color driving laser without further polarization or time delay adjustment. With the increase of single-atom response and the improvement of macroscopic phase-matching [21], the HHG efficiency of a frequency-doubled driving laser is about two orders of magnitude higher than that of the fundamental laser. The ionization rate is

largely increased in two-color field compared to fundamental field, which is dominant in the HHG enhancement. Our numerical calculation result shows that the ionization rate in fundamental field is only about 20% while it is nearly 100% in second-harmonic (SH) field. The enhanced XUV spectral region is related to the time delay between the fundamental and SH pulses.

The output pulses of the secondary compression stage are focused by a concave mirror (f = 500 mm). A BBO (400 μm thickness) is placed at 50 mm before the focus to achieve maximum SH conversion efficiency and reduce excessive self-focusing effect. The frequency doubling efficiency is about 30%. The SH pulses acquire group velocity dispersion of about +140 fs$^2$ more than the fundamental pulses through air and optics during the propagation. Thus, the pulse duration of the SH pulses is estimated to be 30 fs. Both the 1030 nm fundamental laser and the 515 nm SH laser are collimated by a concave mirror (f = 750 mm). The two-color field is naturally orthogonally polarized (p polarized 1030 nm fundamental pulses and s polarized 515 nm SH pulses). By using a true zero-order half-wave plate of 1030 nm laser, the polarization can be tuned to be parallel (s polarized). The two-color field composed by 30 fs SH and 26 fs fundamental pulses is then focused by an f = 200 mm concave mirror and interacts with krypton to generate high-order harmonics. The gas target is a nozzle with a 200 μm diameter pore, and the backing pressure of krypton is about 2 bars.

The fundamental and SH pulses are partially overlapped in time domain at the gas target in the simple collinear setup. Based on the odd-order harmonics we observed, as shown in Fig. 3, and the delay between the SH and fundamental pulses, which is estimated to be over 100 fs during propagation, we infer that only the edges of the SH and fundamental pulses are overlapped. HHG experiments are carried out using a parallelly polarized two-color field, an orthogonally polarized two-color field, and the fundamental field only, respectively. The 10$^{th}$ ~ 22$^{nd}$ order harmonic spectra with energy intervals of 1.2 eV are collected by an MCP/phosphor screen detector and recorded by a CCD camera, as shown in Fig. 3.
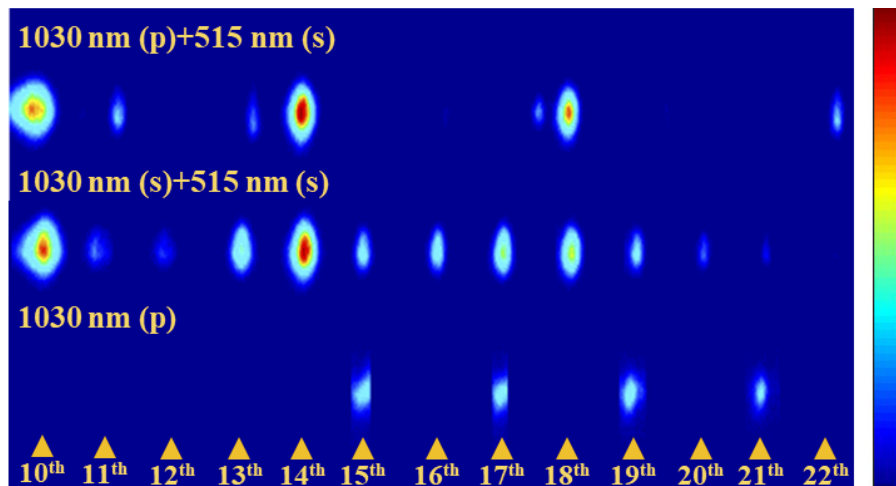


**Fig. 3.** The harmonics generated by different driving fields. Top: orthogonally polarized two-color field. Middle: parallelly polarized two-color field. Bottom: 1030 nm single-color driving field. The top and middle spectra are obtained at 2000V MCP voltage, and the bottom spectrum is obtained at 2600 V.

Harmonics below 10$^{th}$ order can be observed on MCP, but these harmonics are spatially overlapped with the second-order diffraction of the corresponding higher-order harmonics. Compared with the parallelly polarized two-color field, the HHG spectrum produced by the orthogonally polarized two-color field is enhanced at the 10$^{th}$, 14$^{th}$, 18$^{th}$, and 22$^{nd}$ orders, while

the intensity of other orders is decreased. The 10th and 14th harmonics can be selected by the monochromator without influent by the second-order diffraction. The HHG intensity of the orthogonally polarized two-color field is estimated to be about two orders of magnitude higher than that of the fundamental field, which cannot be observed at 2000V MCP voltage as that of the two-color field HHG. To investigate the HHG at different pulse delays, we build a noncollinear delay stage, as shown in Fig. 4 and Fig. 5. This delay stage is optional and can be removed to use the simple collinear setup.
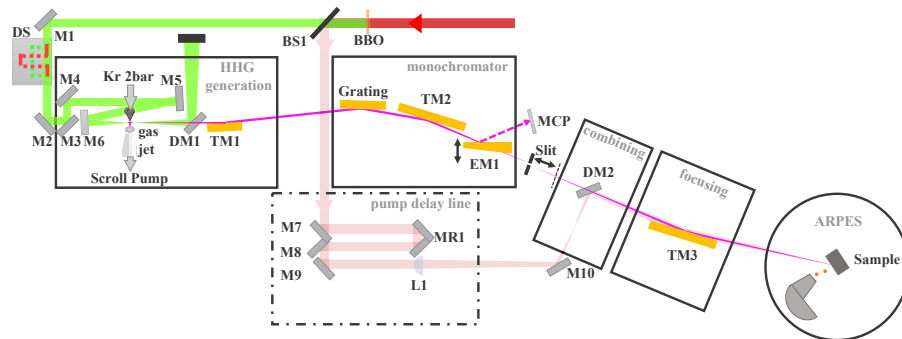


**Fig. 4.** The optical setup of the XUV beamline. M1~M10: femtosecond silver mirror; BS1: beam splitter 5:95; DM1: drilled mirror; TM1~TM3: toroidal mirror; EM1: edge-cutted mirror, which reflects the HHG into the MCP detector when being moved into the beam; L1: a lens system including an f = 300 mm lens, an f = -300 mm lens, and an f = 500 mm lens; MR1: total-reflection reflector. DS: An optional delay stage to tune the delay between the SH and fundamental pulses. The solid-line boxes represent the vacuum chambers.
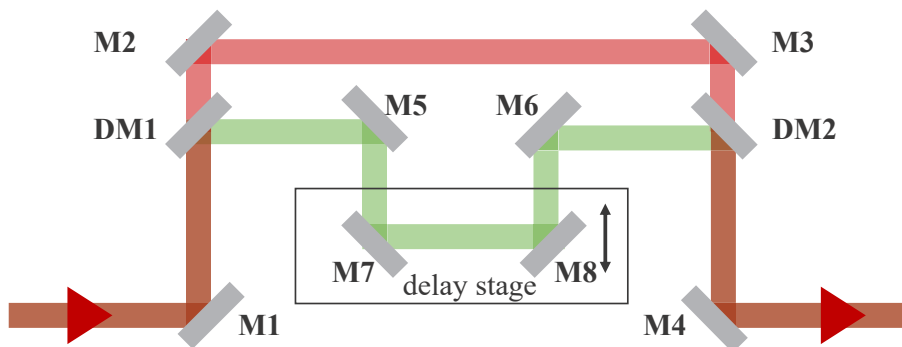


**Fig. 5.** The optical setup of noncollinear coupled two-color field. M1~M8: femtosecond enhanced silver mirrors; DM1~DM2: dichroic mirrors.

The optical setup of the beamline for the generated XUV pulses to transmit to the sample is shown in Fig. 4.

A 3-axis linear stage achieves the movement of the gas target in the HHG chamber, and a gas catcher is installed on another 3-axis linear stage opposite the gas target. The generated XUV is transmitted along with the driving laser to a drilled mirror positioned 200 mm behind the focus at a 45° angle. The diameter of the drilled hole is 1.5 mm. The XUV beam passes through the hole, and most of the driving laser is reflected to a light dump outside the vacuum chamber. Due to the self-focusing in the fused silica plates and the BBO, the profile of the driving laser becomes close to an "annular beam" [27] and its transmission through the drilled hole is minimized. The

laser power through the drilled hole is about 100 mW, and does not affect the optical elements in the XUV beamline. The XUV beam is then collimated by an f = 400 mm toroidal mirror (ARW Optics) and sent to the monochrome chamber. The XUV is separated by an X-ray Czerny-Turner (XCT) monochromator consisting of two gold-coated toroidal mirrors and a flat blazed grating. In the monochromator, the collimated XUV beam is diffracted by a gold-coated grating whose groove density is 150 gr/mm and blazing angle is 2.2°. After diffraction, the XUV is focused to an adjustable exit slit by an f = 300 mm toroidal mirror. A gold-coated flat mirror mounted on a motorized linear positioner is placed in front of the exit slit to let the beam either focus on an MCP detector or go through the exit slit to the combining chamber. In the combining chamber, the IR pump laser from the beam splitter is reflected by a drilled silver-coated mirror, where the XUV beam passes through the 6 mm drilled hole. Finally, a toroidal mirror f = 550 mm is used to image the combined pump and probe beam into the ARPES setup.

The photon flux of a single harmonic before the sample is measured by a photodiode (Optodiode SXUV-100). The highest flux of $2 \times 10^{12}$ phs/s is obtained at 21.6 eV via orthogonally polarized two-color field HHG. The overall transmission efficiency of the XUV beamline is 6%. The reflectance of the gold-coated collimating toroidal mirror at an 87° incident angle placed in the monochromator is estimated to be 90%, the reflectance of the focusing toroidal mirror at an 83° incident angle is estimated to be 80%, the reflectance of the uncoated imaging toroidal mirror at an 87° incident angle after the monochromator is estimated to be 85%, and the transmission efficiency of the grating is estimated to be 10%. Therefore, the generated XUV photon flux at 21.6 eV is about $3 \times 10^{13}$ phs/s. The efficiency may be further improved if we use a driving laser with higher pulse energy at a higher repetition rate, which can help us to avoid the tight-focusing geometry.

## 3.　Vacuum design of the XUV beamline

The ARPES measurement requires an ultra-high vacuum environment better than $1 \times 10^{-10}$ mbar. Differential pumping structures are applied to enhance the vacuum condition in the XUV beamline. The differential pumping is designed via finite element analysis. The vacuum chambers in the beamline are shown in Fig. 4. In the HHG chamber, a gas catcher is installed right below the gas jet. Most Kr atoms from the gas jet after the interaction are removed by a scroll pump (Iwata ISP-500C), and two molecular pumps (Leybold MAG300p) are installed on the HHG chamber to maintain the vacuum to $5.4 \times 10^{-3}$ mbar during experiments. A drilled copper plate with a 6 mm diameter hole replaces the regular copper ring to seal the flange between the HHG and monochromator chambers. When the backing pressure of the gas jet is 3 bars, the vacuum in the HHG chamber is $5.4 \times 10^{-3}$ mbar and in the monochromator is $1.2 \times 10^{-5}$ mbar. Each vacuum chamber, the monochromator, combining or focusing chamber, is installed with a molecular pump (Leybold MAG300p). Another drilled copper plate is placed just behind the exit slit of the monochromator. The exit slit is connected with the chamber by a 100 mm long CF16 bellow. This structure shows an excellent differential pumping behavior that the vacuum in the combining chamber reaches $2.5 \times 10^{-8}$ mbar. The vacuum in the focusing chamber reaches $1 \times 10^{-9}$ mbar during the experiments and the vacuum in ARPES is better than $1 \times 10^{-10}$ mbar.

## 4.　HHG in two-color laser fields

To study the difference of HHG driven by the two-color field with different pulse delays, we build a non-collinear beam coupling interferometer. Its optical setup is shown in Fig. 5.

The time delay is adjusted via a precision linear stage. By adjusting the time delay, conversion efficiency enhancement selectivity among the adjacent harmonics is observed in HHG. When the time delay between a 515 nm pulse and a 1030 nm pulse is close to zero, the intensity of the $18^{th}$ harmonic reaches a minimum, and the intensity of the $17^{th}$ and $19^{th}$ harmonics increases, as shown in Fig. 6. This feature allows an enhancement at a specific order, thus together with the

monochromator, photon energy tunable applications with high photon flux requirements can be performed.
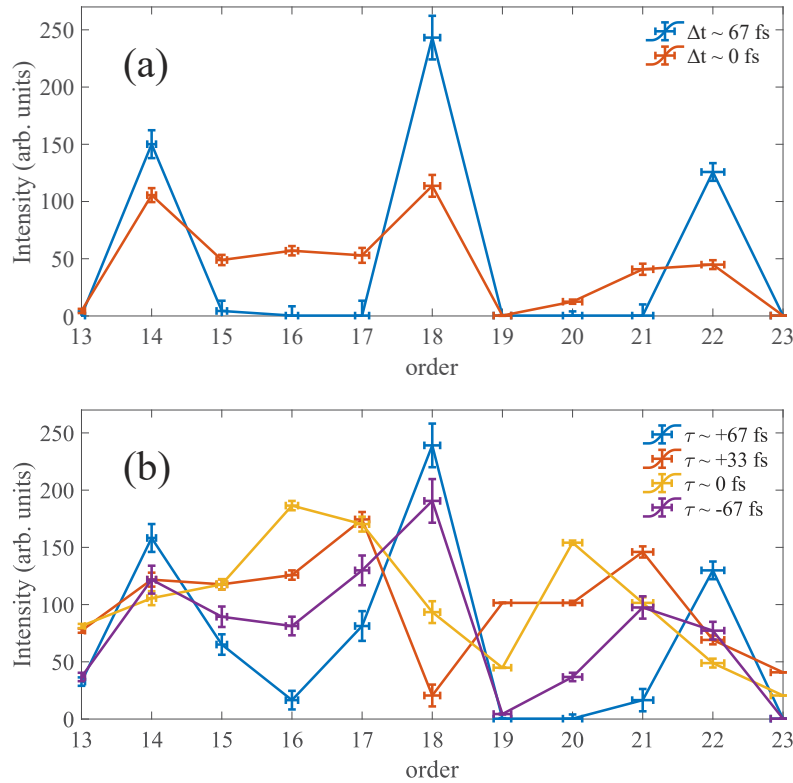


**Fig. 6.** HHG intensity changes with time delay in (a) orthogonal polarized two-color field and in (b) parallel polarized two-color field. τ is the delay between two-color pulses. SH pulse leads fundamental pulse when τ > 0. The HHG spectral shape is almost unchanged in an orthogonal polarized two-color field, while the spectrum varies significantly with the delay in a parallel polarized two-color field. The error bars on the vertical axis are estimated by intensity fluctuation measured by the photodiode, and on the horizontal axis are estimated by the resolution of the detector and the spot size on the phosphor screen.

The highest photon flux is obtained in an orthogonal polarized two-color field when the fundamental pulse and SH pulse are slightly overlapped. By slightly turning the angle of the BBO crystal, the intensity distribution at τ ~ 0 fs is adjusted, and the spectra of the 16th, 17th, 18th, and 19th selectively enhanced harmonics are observed, as shown in Fig. 7. When the BBO crystal is slightly rotated, the intensity of SH pulses decreases and the intensity of fundamental pulses increases, while the two-color field phase difference is also changed. The changes of the field shape lead to different single-atom response which changes the harmonic spectrum [28]. These changes allow the enhancement to either even harmonics (e.g., 18th) or odd harmonics of fundamental wave (e.g., 17th order) or SH wave (e.g., 16th order). The selective enhancement occurs in both parallel-polarized and orthogonal polarized two-color fields and produces a high-flux wavelength-tunable XUV source.

At Δt ~ 0, a significant bandwidth extension is observed in the parallel-polarized two-color field. As shown in Fig. 8, the harmonic intensities at 25~35 orders are enhanced to above $10^{10}$ phs/s, extending the wavelength-tunable range of the EUV source.
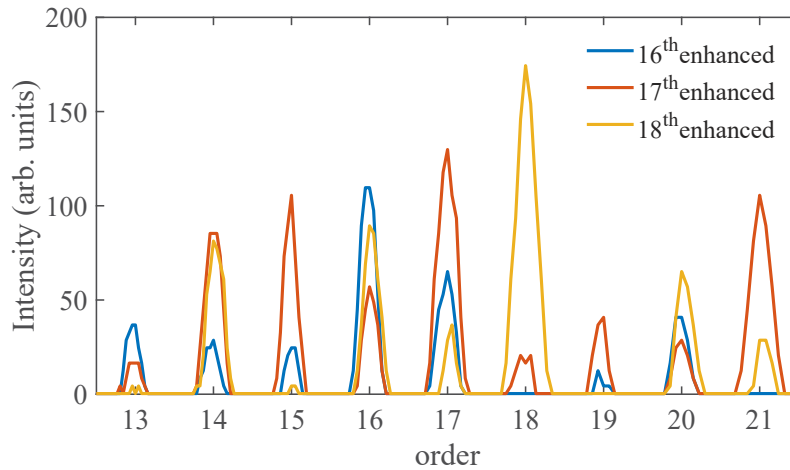
**Fig. 7.** HHG spectrum changes when slightly turning the angle of BBO (5°) at τ~ 0 fs in the orthogonal polarized two-color field. The 18th harmonic is enhanced at 0°, while the 17th and 16th harmonic enhancements are observed in turn when turning the angle of BBO from 0° to 5°.
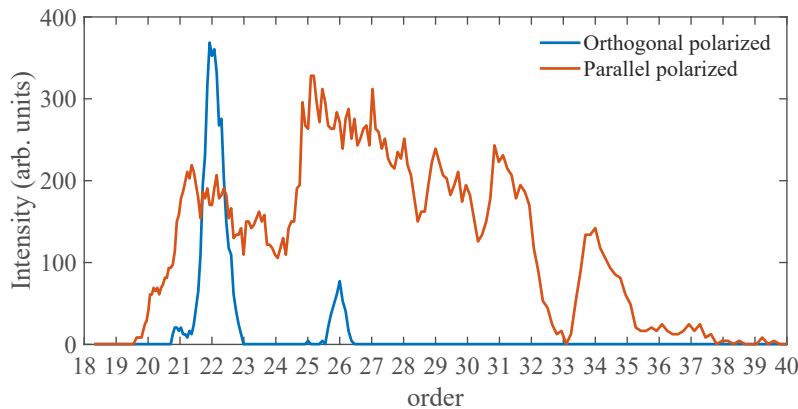


**Fig. 8.** The harmonic intensity of the orthogonal polarized and parallel polarized two-color fields which is measured at τ~ 0 fs.

We numerically simulated the HHG spectrum using a strong-field approximation [29]. The result is shown in Fig. 9, which shows that to enhance the harmonic at 25~35 orders, the SH pulse should lead the fundamental pulse to get a higher ionization rate, then the ionized electrons are accelerated in the asymmetric electric field of a two-color driving pulse to get larger kinetic energies [30]. This enhancement is a combination of pulse delay and phase delay control of the two-color field. The pulse delay is essential to adjust the ionization and the phase delay is to ensure the acceleration in a two-color field [21]. Therefore, the pulse delay decides the HHG spectrum shape which is not changed by the phase delay. The highest harmonic intensity is obtained at +13.7 fs, which is about half of the pulse duration. If the SH pulse is ahead of the fundamental pulse by more time, the enhancement region moves to lower photon energies. While if the fundamental pulse leads the SH pulse, the enhancement becomes small and the HHG spectrum gradually turns into the spectrum produced by SH pulses and fundamental pulses separately. The phase delay is critical in enhancing the HHG intensity near the cut-off by adjusting the single atom response. Simulation results show that the best phase delay to enhance
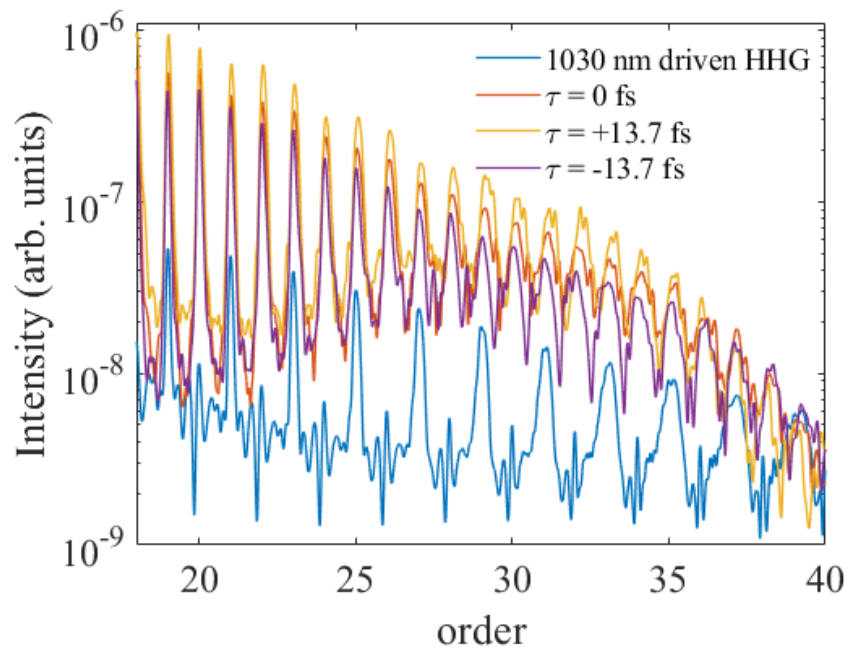
**Fig. 9.** The simulated HHG spectra of two-color field at different delays (red line: $\tau = 0$ fs; yellow line:$\tau = + 13.7$ fs; purple line:$\tau = -13.7$ fs) and fundamental field (blue line).
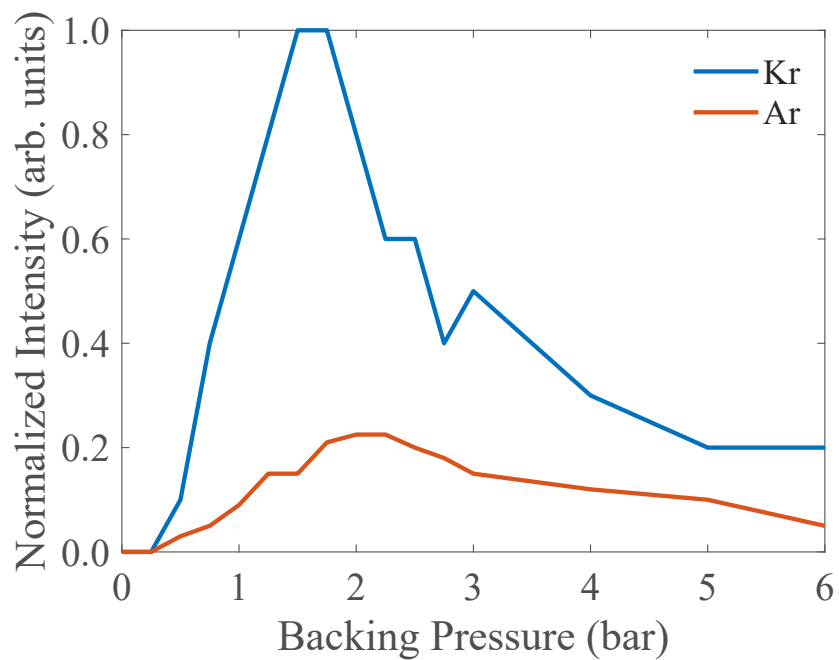


**Fig. 10.** The harmonic intensity of the $18^{th}$ harmonic changes with backing pressure in Krypton and in Argon, respectively. Blue line: in Krypton; Red line: in Argon.

the harmonics at 25~35 orders is π/2, and the enhancement is much smaller if the phase delay is 0, which means the enhancement is partly due to the asymmetric field shape but not merely the field enhancement.

The change of HHG intensity with backing pressure is also tested when krypton and argon are used separately, as shown in Fig. 10. The maximum intensity of the 18th harmonic in argon is about 20% that of krypton.

This wavelength tunable XUV source has advantages for the investigations of three-dimensional materials which need tunable photon energies to detect different momentum at normal direction.

## 5. Energy/time resolution tunable design of XUV beamline

A monochromator is applied to select a particular order of harmonics in the XUV beamline. The grating introduces pulse front tilt, which greatly reduces the time resolution of the system. The OPM scheme can reduce the pulse front tilt but results in poor energy resolution and narrow bandwidth. Meanwhile, the high photon flux leads to a significant space charge effect, which further reduces the energy resolution. A grating monochromator using a CDM scheme is suitable to obtain a high energy resolution and a wide bandwidth, but it leads to a large pulse front tilt. In this setup, we designed a spatial filtering method to adjust the time resolution using a CDM scheme, which is realized by adjusting the axial position of the exit slit.

### 5.1. Adjustment of energy resolution of the XUV source

The energy resolution of the XUV source is evaluated by measuring the Fermi edge of a bulk gold sample. The bandwidth of the 18th harmonic is about 110 meV, which is broader than the spectrum selected by the monochromator.

The energy resolution of the HHG-ARPES system is determined by the resolution of the monochromator $\Delta E_m$, the resolving power of the grating $\Delta E_g$, the resolution of ARPES $\Delta E_{ARPES}$ and the energy shift caused by the space charge effect $\Delta E_{SC}$. The detailed derivations are shown in Appendix A. The energy resolution of the HHG-ARPES system $\Delta E_s$ is expressed as:

$$\Delta E_s = \sqrt{\Delta E_m^2 + \Delta E_g^2 + \Delta E_{ARPES}^2 + \Delta E_{SC}^2}. \tag{1}$$

Ultrafast XUV pulses with a large number of photons can produce a significant space charge effect even if at a high repetition rate, which has been observed experimentally [14]. To model the space charge effect, we consider an electron pulse generated by photoionization. Considering an XUV pulse with pulse duration τ, electrons are excited at the surface of a metal sample such as Au. The earliest excited electron moves a distance determined by the maximum kinetic energy and pulse duration when the latest electron is excited, which is on the order of ~100 nm. The XUV spot size is ~100 μm so the electron cloud has a shape of flat disc. The electrons interact with each other during the electron pulse propagation via Coulomb force. The electrons with kinetic energy near the fermi edge bring additional kinetic energies in all directions, so the kinetic energy is broadened. Meanwhile, the electrons with kinetic energy away from the fermi edge lagged during the propagation. As a result, these electrons push forward the electrons with kinetic energy near the fermi edge, which causes the fermi edge shift as well as the energy broadening. The final kinetic energy change of the photoelectrons is obtained by the formula $\Delta E_k = m_e v^2/2 - m_e v_0^2/2$, where $m_e$ is the mass of an electron, v is the final speed of the monitored electron, and $v_0$ is its initial velocity. Considering the monitored electrons with an initial kinetic energy equal to the fermi energy, their final kinetic energies are different due to the space charge effect, so their kinetic energy changes $\Delta E_k$ are different. The distribution of $\Delta E_k$ is used to derive the energy broadening of the space charge effect, $\Delta E_{SC} = \Delta(\Delta E_k)$. The Fermi energy shift is the average value of $\Delta E_k$. The process is examined via numerical simulation with the Monte Carlo method. The detailed description is shown in Appendix B.

The kinetic energy change depends on the photon flux per pulse linearly, and is reciprocal of XUV spot size. The energy resolution changed by different XUV pulse duration is negligible because the beam radius is much larger than the flight distance of electrons in its pulse duration. The simulation results are shown in Fig. 11, which is consistent with the reported experiment results [19,20]. The space charge effect is almost independent to the XUV photon energy, as shown in Fig. 11(a) and 11(b). The space charge effect at the 650 μm spot diameter is about 10 times smaller than at 100 μm. It is worth noticing that although the XUV pulse parameter in Liu's experiment [14] is almost the same as in Cucini's experiment [20], the space charge effect in Liu's experiment is much more significant than in Cucini's experiment and our theoretical prediction. That might be due to the excessive lower-order harmonics passing through the aluminum filter in Liu's experiment, which does not exist in Cucini's monochromator design. There are several studies that describe the space charge effect analytically or numerically [31,32,33]. We use a simplified ionization spectrum from the measurement, instead of a rectangular energy distribution as in Ref. [33]. Our results show that the mirror positive charges almost do not affect the energy broadening and the Fermi energy shift, and they tend to produce photoelectrons with higher or lower kinetic energies than without positive charges. The fastest photoelectrons pass over the intrinsic distances of the electrons within 1 picosecond, and the influence of positive charges can be ignored in ~100 ps scale. In our model, we use a 1 ps time step for the first 62.4 ps propagation, then a 10 ps time step for the following 624 ps propagation, and finally a 100 ps time step for the last 6.24 ns propagation instead of a fixed time step.
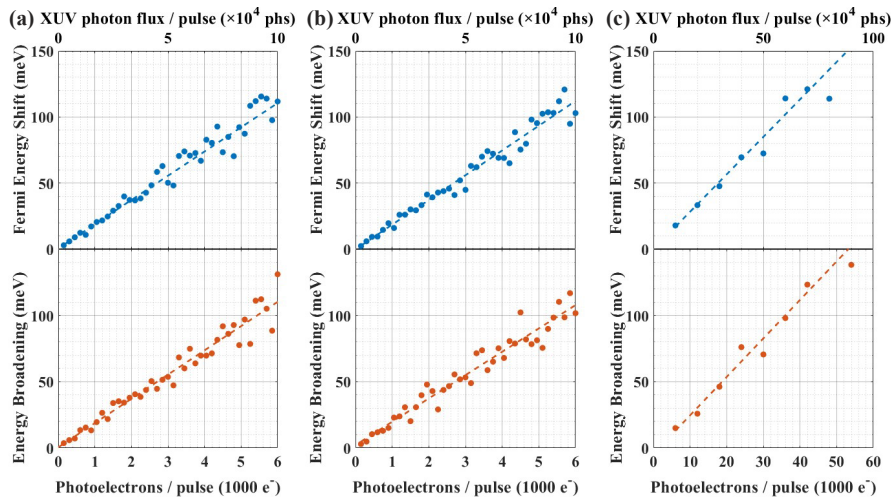


**Fig. 11.** The numerical simulation results of the Fermi energy shift and the energy broadening due to the space charge effect. Blue dots: Fermi energy shift simulated in the Monte Carlo method; Blue dashed lines: linear fitting to the simulation results of the Fermi energy shift. Red dots: energy broadening simulated in the Monte Carlo method; Red dashed lines: linear fitting to the simulation results of the energy broadening. (a) The Fermi Energy shift and energy broadening at 16.8 eV and 100 μm spot diameter; (b) at 21.6 eV and 100 μm spot diameter; (c) at 21.6 eV and 650 μm spot diameter.

Both our simulation and experimental results indicate that the photon flux at 21.6 eV should be reduced to about $1 \times 10^9$ phs/s, or $2.5 \times 10^3$ phs per pulse, in order to avoid the space charge effect. Enlarging the XUV spot size can effectively reduce the space charge effect. However, the decreasing XUV intensity makes the pump-probe process more difficult to happen. So the XUV spot size needs to be controlled to balance the pump-probe signal and the space-charge effect. In our experiment, we find the best XUV spot radius is about 100 μm. Under the condition of low

photon flux, the energy resolution of the system is mainly determined by the resolution of the monochromator and the resolution of the ARPES. The calculated energy resolution of the XUV source in our system is better than 60 meV, but it is not realized because we move the exit slit of the monochromator out of focal plane to get a better time resolution. In current setup, the energy resolution in our system is 96 meV, while the energy resolution of ARPES is about 40 meV (at 10 eV pass energy and 1.5 mm slit width).

### 5.2. Adjustment of time resolution of the XUV source

Increasing the number of illuminated grooves improves energy resolution and causes a pulse front tilt [34]. The full-width-half-maximum (FWHM) pulse front tilt caused by grating diffraction of a Gaussian profiled beam can be estimated as [13]:

$$\Delta t_{pulse-front\ tilt} = \frac{2ln2}{\pi}\frac{\lambda}{c}S\frac{\sigma_{OPM}}{cos\alpha} \approx 0.44\frac{\lambda N}{c}, \tag{2}$$

where $N = S\frac{\sigma_{OPM}}{cos\alpha}$ is the total number of illuminated grooves. The time-resolution of the beamline can be expressed as $\Delta t_{beamline} = [\Delta t_{pulse-front\ tilt}{}^2 + \Delta t_{XUV}{}^2 + \Delta t_{pump}{}^2]^{(1/2)}$, where $\Delta t_{XUV}$ is the intrinsic pulse duration of XUV and $\Delta t_{pump}$ is the pulse duration of the pump laser. The pulse front tilt is caused by the different optical paths at different axial positions on the grating. The direction of a diffraction beam is different from the direction of the reflection so the pulse front is tilted in order to keep the optical path the same for different rays as shown in Fig. 12. If the exit slit is away from the focal plane, or if an additional slit is added away from the focal plane, the pulse front tilt can be effectively reduced. The slit is then considered as a spatial filter. Because the optical path and the pulse front of a diffraction beam are spatial dependent, a spatial filter that selects only a part of the beam can reduce the influence of the pulse front tilt.

When the exit slit of the monochromator is placed away from the focus plane and the slit width is reduced, both space charge effect and pulse front tilt are reduced. Numerical results show that when the exit slit is placed at z = 6 mm and the slit width is reduced to 1/10 of the beam diameter, the pulse front tilt is reduced from 230 fs to 40 fs. In this condition, the photon flux remains about 17% in our calculation. The minimum time resolution of the system is ~100 fs. The time broadening is caused by the dispersion of the optical path at different wavelengths after the grating, the pulse front tilt and the pump pulse duration. Meanwhile, the energy resolution without space charge effects is ~95 meV, which is slightly smaller than the bandwidth of the 18th harmonic (about 110 meV) for the XUV source. In our calculations, if the slit width is further reduced, the energy and time resolution does not change, but the space charge effect can be further reduced. Our experimental results show a good agreement with the calculations. The XUV flux was measured with an XUV photodiode in front of the sample. The XUV photocurrent from the high-order harmonics driven by the orthogonally polarized two-color field at 21.6 eV without the use of a waveplate is 250 nA, corresponding to a flux estimated to be ~$2 \times 10^{12}$ phs/s using a photoelectron conversion efficiency of 0.04 A/W. The energy resolution measurement was achieved by testing the Fermi edge of polycrystalline gold at low temperature. Fermi fringes were measured at ~10 K using harmonics of 21.6 eV. The resulting FWHM was 96 meV at $5 \times 10^9$ phs/s and 110 meV at $5 \times 10^{10}$ phs/s. The temporal resolution was measured by pump-probe experiments. The pump light is a 1030 nm laser with a pulse width of 60 fs. Our experimental results show a time resolution of ~110 fs. Further improvement of the beamline can be achieved by applying an additional slit after the exit slit. In this setup, the exit slit is used to adjust the energy resolution, while the additional slit can be used to adjust the temporal resolution. In our calculations, when the width of the exit slit is reduced to the waist spot diameter at the focal plane of the monochromator and the width of the additional slit is reduced to 1/10 of the beam diameter, the pulse front tilt is reduced to ~23 fs with a temporal resolution of ~46 fs and an energy resolution of ~59 meV@21.6 eV when the pulse duration of the pump is 25fs. And the

energy resolution at 16.8 eV reaches 45 meV while the time resolution reaches 68 fs. If the grating groove density is changed to 300 gr/mm, a high energy resolution of ~23 meV and high time resolution ~85fs can be achieved at 16.8 eV. This means our monochromator scheme can achieve a high energy resolution regardless of the parameters of the driving laser while showing a good time resolution. Thus a high efficiency HHG driven by short pulses and a high energy/time resolution beamline can be separately designed. Theoretically, the pulse front tilt can be infinitely reduced by applying an even smaller slit width. Due to the high photon flux of this HHG source, another scheme that totally eliminate the pulse front tilt by applying an additional grating with the same parameter after the monochromator is also possible.
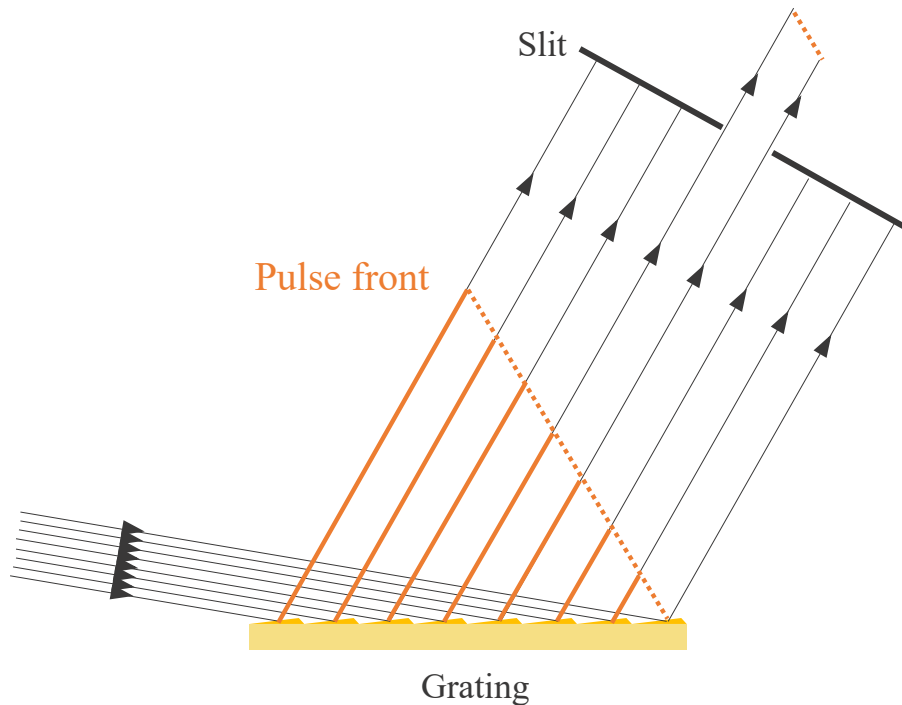


**Fig. 12.** Diagram of pulse front tilt.

## 6. Conclusions

In summary, we develop an XUV source for Tr-ARPES with a tunable range of 12~40.8 eV and high photon flux of $2 \times 10^{12}$ phs/s at sample at 21.6 eV with the help of a 150 gr/mm CDM grating. The high flux is achieved by a combination of high HHG efficiency driven by two-color pulses and high transmission efficiency of our beamline. The simple and compact CDM monochromator achieves a relatively high transmission with only grazing reflection on the optics and without a metal filter, while the pulse front tilt effect can be controlled and reduced by the out-of-focus slits. In the vacuum design of the XUV beamline, the differential pumping shows great advantage in the extremely high vacuum obtained in the ARPES.

We use the two-color field to generate high-order harmonics at a high efficiency, which is not yet used in other Tr-ARPES beamlines. A significant enhancement about two orders of magnitude in the two-color field is observed compared to the fundamental driving case due to the increased ionization rate. Numerical results show that the phase delay of the two-color field determines the single-atom response in the asymmetric driving field. The enhanced harmonic can be tuned

from the 18$^{th}$ to the 17$^{th}$ or 16$^{th}$ order, by adjusting the phase delay between two-color pulses by slightly rotating the BBO crystal. The HHG spectrum is significantly affected by the ionization, and can be adjusted by the pulse delay of the two-color field. A significant enhancement at 25~35 orders is also observed in a parallel polarized two-color field by adjusting the pulse delay to nearly 0 fs. Numerical results show that the most efficient enhancement is at τ=13.7fs with a phase delay π/2. These results allow photon-energy adjusting with high-photon flux.

Furthermore, we investigate the energy and time resolution of the HHG-ARPES system. Especially, we investigate the space charge effect and the pulse front tilt. We model the space charge effect and give the numerical simulation results in the Monte Carlo method, which shows a way to predict the energy resolution in an experiment using a high-flux pulsed XUV source. A new method that uses a spatial filter to reduce the pulse front tilt is carried out. By moving the exit slit of the monochromator away from the focal plane, the temporal resolution is improved to 110 fs while the energy resolution is 96 meV. An additional slit placed away from the focus plane can efficiently reduce the pulse front tilt produced by the monochromator and bring better results. The simulation shows the energy resolution at 21.6 meV can reach 59 meV while the time resolution can reach 46 fs. The energy resolution at 16.8 eV can also reach 45 meV while the time resolution can reach 68 fs. This scheme has a potential to achieve both tunable high energy resolution and high time resolution with a large wavelength tunable range using a single grating. Details of the time-resolved ARPES measurement will be presented elsewhere [35].

This XUV beamline with adjustable wavelength, energy resolution and time resolution enables the study of materials with requirements of depth selectivity, high energy resolution or high time resolution.

## Appendix A: Resolution of a CDM monochromator

The resolution of a monochromator mounted with classical diffraction is determined by the degree of spectral divergence and the width of the exit slit, and can be calculated by the following formula [13]:

$$\Delta\lambda_c = S\frac{cos\beta}{|m|q\sigma_c}, \tag{3}$$

where S is the width of the exit slit, β is the diffraction angle, m is the diffraction order, $\sigma_c$ is the groove density of the grating and q is the length of the exit arm of the monochromator, respectively.

The XUV bandwidth is also affected by the grating resolution [36]:

$$\Delta\lambda_g = \frac{\lambda}{|m|N}, \tag{4}$$

where λ is the center wavelength of a selected harmonic, and N is the total groove number of the grating in the region illuminated by XUV, which is related to the diameter of the incident beam:

$$N = \frac{\sigma_c D}{cos\alpha}, \tag{5}$$

where α is the incident angle and D is the diameter of the collimated beam before the grating.

The energy resolution of the monochromator and the resolving power of the grating can be expressed as:

$$\Delta E_m = 2\pi ch\frac{\Delta\lambda_c}{\lambda^2}, \tag{6}$$

$$\Delta E_g = 2\pi ch\frac{\Delta\lambda_g}{\lambda^2}. \tag{7}$$

The energy resolution of the ARPES can be expressed as [19]:

$$\Delta E_{ARPES} = E_p \cdot d_s / 2R_0, \tag{8}$$

where $E_p$ is the pass energy, $d_s$ is the entrance slit width and $R_0$ is the hemisphere radius.

## Appendix B: Kinetic energy change of the photoelectrons caused by space charge effect

Considering an XUV pulse arrives at the sample surface of a sputtered Au, the total number of photoelectrons depends on the single photon ionization probability, which is proved to be 0.06 $e^-$/photon [19]. The electron cloud is considered to have a Gaussian profile in either of the three dimensions in space. The radial distribution is determined by the spot radius of the XUV beam and the axial distribution is determined by the kinetic energy of the electrons. To simplify our model, an average kinetic energy is applied in construction of the electron distribution:

$$E_k = E_{xuv} - E_{sample}, \tag{9}$$

$$E_{average} = E_k / 2, \tag{10}$$

where $E_k$ is the maximum initial kinetic energy for a given XUV photon energy $E_{XUV}$ and the ionization energy of the sample $E_{sample}$ (5.31 eV for sputter cleaned Au [37]), and $E_{average}$ is the average kinetic energy.

The kinetic energy of the photoelectrons E is distributed from 0 to $E_k$ depends on the photoemission spectrum of the selected XUV photon energy. The kinetic energy distribution is simplified from the photoemission spectra tested in Ref. [20]. The initial velocity $v_0$ of the photoelectrons can be expressed as:

$$v_0 = \sqrt{2E/m_e}, \tag{11}$$

where $m_e$ is the mass of an electron. The initial positions of the photoelectrons are randomly allocated within the given Gaussian distribution, so that the initial velocities of the photoelectrons also have a randomly distribution. However, not all of the electrons flight directly towards the entrance of ARPES. Here, the electron emission is considered as a cosine radiation, and the direction of the electron movements are uniformly distributed in ±90 degree.

Then the electron-electron interaction for an electron marked as p can be described as:

$$F_{\hat{x},\hat{y},\hat{z}}(p) = \sum_{p' \neq p} -\frac{e^2}{4\pi\varepsilon_0 L(p,p')^2} \cdot \frac{[x,y,z](p') - [x,y,z](p)}{L(p,p')}, \tag{12}$$

where L is the distance between electron p and p', x, y, and z are the spatial positions at the $\hat{x}$, $\hat{y}$, *and* $\hat{z}$ direction of the electron p and p', e is the charge of single electron, and $\varepsilon_0$ is the permittivity of vacuum. The velocity changes due to the Coulomb force in a short time $\Delta t$ can be expressed as:

$$\Delta v_{\hat{x},\hat{y},\hat{z}}(p) = \frac{F_{\hat{x},\hat{y},\hat{z}}(p)\Delta t}{m_e}. \tag{13}$$

And the position changes of the photoelectrons are:

$$\Delta[x,y,z](p) = [x,y,z](p) + (v_{0\hat{x},\hat{y},\hat{z}}(p) + \Delta v_{\hat{x},\hat{y},\hat{z}}(p)) \cdot \Delta t. \tag{14}$$

Then we employ a Monte Carlo simulation to obtain the final velocity of the photoelectrons $v_{\hat{x},\hat{y},\hat{z}}(p)$, and its corresponding kinetic energy change:

$$\Delta E(p) = \sum_{\hat{x},\hat{y},\hat{z}} \frac{1}{2} m_e (v_{\hat{x},\hat{y},\hat{z}}(p)^2 - v_{0\hat{x},\hat{y},\hat{z}}(p)^2). \tag{15}$$

## References

1. C.-M. Lee, T. Rohwer, E. J. Sie, A. Zong, E. Baldini, J. Straquadine, P. Walmsley, D. Gardner, Y. S. Lee, I. R. Fisher, and N. Gedik, "High resolution time- and angle-resolved photoemission spectroscopy with 11 eV laser pulses," Rev. Sci. Instrum. **91**(4), 043102 (2020).

2. H. Hedayat, C. J. Sayers, A. Ceraso, J. van Wezel, S. R. Clark, C. Dallera, G. Cerullo, E. D. Como, and E. Carpene, "Investigation of the non-equilibrium state of strongly correlated materials by complementary ultrafast spectroscopy techniques," New J. Phys. **23**(3), 033025 (2021).

3. J. Madéo, M. K. L. Man, C. Sahoo, M. Campbell, V. Pareek, E. Laine Wong, A. Al-Mahboob, N. S. Chan, A. Karmakar, B. M. K. Mariserla, X.-Q. Li, T. F. Heinz, T. Cao, and K. M. Dani, "Directly visualizing the momentum-forbidden dark excitons and their dynamics in atomically thin semiconductors," Science **370**(6521), 1199–1204 (2020).

4. M. Shoji, K. Kaniwa, Y. Hiranuma, O. Maselli, and F. Mafuné, "Solvation Structure of I$^-$ and Na$^+$ on the Surface of NaI Aqueous Solution Studied by Photodetachment Spectroscopy in Combination with Mass Spectrometry," Phys. C (Amsterdam, Neth.) **115**(11), 2148–2154 (2011).

5. M. Okawa, K. Ishizaka, H. Uchiyama, H. Tadatomo, T. Masui, S. Tajima, X.-Y. Wang, C.-T. Chen, S. Watanabe, A. Chainani, T. Saitoh, and S. Shin, "Bulk-sensitive laser-ARPES study on the cuprate superconductor YBa$_2$Cu$_3$O$_{7-\delta}$," Phys. C **470**(S1), S62–S64 (2010).

6. H. Tanaka, Y. Fujisawa, K. Kuroda, R. Noguchi, S. Sakuragi, C. Bareille, B. Smith, C. Cacho, S. W. Jung, T. Muro, Y. Okada, and T. Kondo, "Three-dimensional electronic structure in ferromagnetic Fe$_3$Sn$_2$ with breathing kagome bilayers," Phys. Rev. B **101**(16), 161114 (2020).

7. Z. Nie, I. C. E. Turcu, and Y. Li, *et al.*, "Spin-ARPES EUV Beamline for Ultrafast Materials Research and Development," Appl. Sci. **9**(3), 370 (2019).

8. K. Kuroda, M. Ochi, H S Suzuki, M. Hirayama, M. Nakayama, R. Noguchi, C. Bareille, S. Akebi, S. Kunisada, T. Muro, M D Watson, H. Kitazawa, Y. Haga, T K Kim, M. Hoesch, S. Shin, R. Arita, and T. Kondo, "Experimental Determination of the Topological Phase Diagram in Cerium Monopnictides," Phys. Rev. Lett. **120**(8), 086402 (2018).

9. E. J. Sie, T. Rohwer, C.-M. Lee, and N. Gedik, "Time-resolved XUV ARPES with tunable 24–33 eV laser pulses at 30 meV resolution," Nat. Commun. **10**(1), 3535 (2019).

10. M. H. Berntsen, O. Gotberg, and O. Tjernberg, "An experimental setup for high resolution 10.5 eV laser-based angle-resolved photoelectron spectroscopy using a time-of-flight electron analyzer," Rev. Sci. Instrum. **82**(9), 095113 (2011).

11. Y. He, I. M. Vishik, M. Yi, S. Yang, Z. Liu, J. J. Lee, S.-D. Chen, S. N. Rebec, D. Leuenberger, A. Zong, C. M. Jefferson, R. G. Moore, P. S. Kirchmann, A. J. Merriam, and Z. Shen, "Invited article: high resolution angle resolved photoemission with tabletop 11 eV laser," Rev. Sci. Instrum. **87**(1), 011301 (2016).

12. F. Y. Bruno, A. Tamai, Q. S. Wu, I. Cucchi, C. Barreteau, A. de la Torre, S. McKeown Walker, S. Riccò, Z. Wang, T. K. Kim, M. Hoesch, M. Shi, N. C. Plumb, E. Giannini, A. A. Soluyanov, and F. Baumberger, "Observation of large topologically trivial Fermi arcs in the candidate type-II Weyl semimetal WTe$_2$," Phys. Rev. B **94**(12), 121112 (2016).

13. L. Poletto and F. Fabio, "Single-Grating Monochromators for Extreme-Ultraviolet Ultrashort Pulses," Appl. Sci. **3**(1), 1–13 (2012).

14. Y. Liu, J. E. Beetar, M. M. Hosen, G. Dhakal, C. Sims, F. Kabir, M. B. Etienne, K. Dimitri, S. Regmi, Y. Liu, A. K. Pathak, D. Kaczorowski, M. Neupane, and M. Chini, "Extreme ultraviolet time- and angle-resolved photoemission setup with 21.5 meV resolution using high-order harmonic generation from a turn-key Yb:KGW amplifier," Rev. Sci. Instrum. **91**(1), 013102 (2020).

15. I. Matsuda and Y. Kubota, "Recent Progress in Spectroscopies Using Soft X-ray Free-electron Lasers," Chem. Lett. **50**(7), 1336–1344 (2021).

16. I. J. Kim, G. H. Lee, S. B. Park, Y. S. Lee, T. K. Kim, and C. H. Nam, "Generation of submicrojoule high harmonics using a long gas jet in a two-color laser field," Appl. Phys. Lett. **92**(2), 021125 (2008).

17. J. Luo, Y. Li, Z. Wang, L. He, Q. Zhang, P. Lan, and P. Lu, "Efficient supercontinuum generation by UV-assisted midinfrared plasmonic fields," Phys. Rev. A **89**(2), 023405 (2014).

18. R. Klas, A. Kirsche, M. Gebhardt, J. Buldt, H. Stark, S. Hädrich, J. Rothhardt, and J. Limpert, "Ultra-short-pulse high-average-power megahertz-repetition-rate coherent extreme-ultraviolet light source," PhotoniX **2**(1), 4 (2021).

19. J. H. Buss, H. Wang, Y. Xu, J. Maklar, F. Joucken, L. Zeng, S. Stoll, C. Jozwiak, J. Pepper, Y.-D. Chuang, J. D. Denlinger, Z. Hussain, A. Lanzara, and R. A. Kaindl, "A setup for extreme-ultraviolet ultrafast angle-resolved photoelectron spectroscopy at 50-kHz repetition rate," Rev. Sci. Instrum. **90**(2), 023105 (2019).

20. R. Cucini, T. Pincelli, and G. Panaccione, *et al.*, "Coherent narrowband light source for ultrafast photoelectron spectroscopy in the 17–31 eV photon energy range," Struct. Dyn. **7**(1), 014303 (2020).

21. M. Puppin, Y. Deng, C. W. Nicholson, J. Feldl, N. B. M. Schröter, H. Vita, P. S. Kirchmann, C. Monney, L. Rettig, M. Wolf, and R. Ernstorfer, "Time- and angle-resolved photoemission spectroscopy of solids in the extreme ultraviolet at 500 kHz repetition rate," Rev. Sci. Instrum. **90**(2), 023104 (2019).

22. D. Bresteau, C. Spezzani, and O. Tcherbakoff, *et al.*, "FAB10: a user-oriented bandwidth-tunable extreme ultraviolet lightsource for investigations of femtosecond to attosecond dynamics in gas and condensed phases," *Eur. Phys. J. Spec. Top.* 1, (2023).

23. J. Rothhardt, M. Krebs, S. Hädrich, S. Demmler, J. Limpert, and A. Tünnermann, "Absorption-limited and phase-matched high harmonic generation in the tight focusing regime," New J. Phys. **16**(3), 033022 (2014).

24. P. He, Y. Liu, K. Zhao, H. Teng, X. He, P. Huang, H. Huang, S. Zhong, Y. Jiang, S. Fang, X. Hou, and Z. Wei, "High-efficiency supercontinuum generation in solid thin plates at 0.1 TW level," Opt. Lett. **42**(3), 474 (2017).

25. Y. Gao, X. Wang, X. Zhu, K. Zhao, H. Liu, Z. Wang, S. Fang, and Z. Wei, "Quantification and analysis of the nonlinear effects in spectral broadening through solid medium of femtosecond pulses by neural network," Phys. Rev. Res. **4**(1), 013035 (2022).

26. S. Xu, J. Wang, Y. Gao, C. Yun, K. Zhao, J. Zhu, S. Fang, and Z. Wei, are preparing a manuscript to be called "Generation of 1.9-cycle pulses with 400 kHz repetition rate at 1030 nm by two-stage solid thin plates."

27. J. Peatross, J. L. Chaloupka, and D. D. Meyerhofer, "High-order harmonic generation with an annular laser beam," Opt. Lett. **19**(13), 942 (1994).

28. S. D. C. Roscam Abbing, F. Campi, A. Zeltsi, P. Smorenburg, and P. M. Kraus, "Divergence and efficiency optimization in polarization-controlled two-color high-harmonic generation," Sci. Rep. **11**(1), 24253 (2021).

29. E. Priori, G. Cerullo, M. Nisoli, S. Stagira, S. De Silvestri, P. Villoresi, L. Poletto, P. Ceccherini, C. Altucci, R. Bruzzese, and C. de Lisio, "Nonadiabatic three-dimensional model of high-order harmonic generation in the few-optical-cycle regime," Phys. Rev. A **61**(6), 063801 (2000).

30. A. Mandal, P. C. Deshmukh, and K. P. Singh, "Controlling high harmonic generation using inhomogeneous two-color driving laser pulse," Laser Phys. **31**(7), 075302 (2021).

31. B. J. Siwick, J. R. Dwyer, R. E. Jordan, and R. J. Dwayne Miller, "Ultrafast electron optics: Propagation dynamics of femtosecond electron packets," J. Appl. Phys. (Melville, NY, U. S.) **92**(3), 1643–1648 (2002).

32. J. P. Long, B. S. Itchkawitz, and M. N. Kabler, "Photoelectron spectroscopy of laser-excited surfaces by synchrotron radiation," J. Opt. Soc. Am. B **13**(1), 201–208 (1996).

33. S. Hellmann, K. Rossnagel, M. Marczynski-Bühlow, and L. Kipp, "Vacuum space-charge effects in solid-state photoemission," Phys. Rev. B **79**(3), 035402 (2009).

34. D. L. Voronov, R. Cambie, R. M. Feshchenko, E. M. Gullikson, H. A. Padmore, A. V. Vinogradov, and V. V. Yashchuk, "Development of an ultrahigh-resolution diffraction grating for soft x-rays," Proc. SPIE **6705**, 67050E (2007).

35. F. Chen, J. Wang, M. Pan, J. Liu, K. Zhao, C. Yun, T. Qian, Z. Wei, and H. Ding, "Time-resolved ARPES with tunable 12-21.6 eV XUV at 400kHz repetition rate," *Rev. Sci. Instrum.*, submitted for publication.

36. S. Serkez, J. Krzywinski, Y. Ding, and Z. Huang, "Soft x-ray self-seeding simulation methods and their application for the Linac Coherent Light Source," Phys. Rev. ST Accel. Beams **18**(3), 030708 (2015).

37. J. E. Lyon, A. J. Cascio, M. M. Beerbom, and R. Schlaf, "Photoemission study of the poly(3-hexylthiophene)/Au interface," Appl. Phys. Lett. **88**(22), 222109 (2006).